

# Spatial and Temporal Control of Microwave Triggered Chemiluminescence: A Protein Detection Platform

Michael J. R. Previte, Kadir Aslan, and Chris D. Geddes\*

Institute of Fluorescence, Laboratory for Advanced Medical Plasmonics, Medical Biotechnology Center, University of Maryland Biotechnology Institute, 725 West Lombard Street, Baltimore, Maryland 21201

We have combined the principles of microwave circuitry and antenna design and our recent work in microwave-triggered metal-enhanced chemiluminescence to now “trigger” chemically and enzyme-catalyzed chemiluminescent reactions with spatial and temporal control. With this technology platform, we achieve spatial and temporal control of enzyme and chemically catalyzed chemiluminescence reactions to achieve more than 500-fold increases in “on-demand” photon flux from chemically catalyzed chemiluminescent reactions. We also report a 6-fold increase in photon flux from HRP-catalyzed assays on disposable coverslips functionalized with HRP and placed proximal to the substrates modified with thin-film aluminum triangle disjointed “bow-tie” structures. In addition, we demonstrate the applicability of this technology to develop multiplexed or high-throughput chemiluminescent assays. We also demonstrate the clinical and biological relevance of this technology platform by affixing aluminum structures in proximity to HRP protein immobilized on nitrocellulose to improve the sensitivity for this model Western blot scheme by 50-fold. We believe analytical applications that rely on enzyme-catalyzed chemiluminescence, such as immunoassays, may greatly benefit from this new platform technology.

In the past two decades, the use of microwave (Mw) radiation has greatly increased for accelerating reactions in synthetic organic chemistry applications,<sup>1–3</sup> assays,<sup>4–8</sup> and biochemistry.<sup>9–11</sup>

High-frequency oscillating microwave fields, such as those of conventional microwave ovens, can induce the alignment of ion fields or dipoles in materials that can be polarized by the respective electric field. When the dipoles of the material or ion fields cannot precisely follow the oscillations of the electric field, energy is lost in the form of heat through dielectric loss and creates the subsequent heating of the material. Due the efficacy of this heating process, microwave heating is implemented to accelerate chemical reactions, increase yields, and improve reproducibility more effectively than conventional heating.<sup>12,13</sup>

In addition to the increasing growth of microwave-assisted organic synthesis (MAOS) applications,<sup>12</sup> microwave irradiation has also been shown to enhance the rates of enzymatic reactions for biological and clinical applications.<sup>10</sup> Akins and Tuan were the first to suggest that the use of microwaves could enhance the estimation of protein assays.<sup>4</sup> With this work, additional applications have been developed that combine the use of microwaves to improve the detectability, sensitivity, and rapidity of immunoassays.<sup>14–16</sup> Recently, we described a new approach, microwave-triggered metal-enhanced chemiluminescence (MT-MEC), to detect and quantify surface protein concentrations using low-power microwaves (Mw) to “trigger” enzyme and chemically catalyzed chemiluminescent reactions.<sup>14,15</sup> Due to increased reaction rates for the enzyme-catalyzed chemiluminescent surface reactions, the “on-demand” nature of light emission provided substantial improvements in signal-to-noise ratios from the locally, triggered chemiluminescent reactions.<sup>14,15,17</sup> As a result, we have shown that MT-MEC facilitates the quantitation and increased detectability of low concentrations of surface-captured protein. Also the application of low-power microwave pulses accelerate or trigger horseradish peroxidase (HRP) enzyme catalysis on the surfaces of the substrates.<sup>14,15,17</sup>

\* To whom correspondence should be addressed. E-mail: geddes@umbi.umd.edu.

- (1) Sridar, V. *Indian J. Chem., Sect. B: Org. Chem. Inclu. Med. Chem.* **1997**, *36*, 86–87.
- (2) Varma, R. S.; Astrazeneca Research Foundation, Bangalore, India, 2002.
- (3) Caddick, S. *Tetrahedron* **1995**, *51*, 10403–10432.
- (4) Akins, R. E.; Tuan, R. S. *Mol. Biotechnol.* **1995**, *4*, 17–24.
- (5) Croppo, G. P.; Visvesvara, G. S.; Leitch, G. J.; Wallace, S.; Schwartz, D. A. *Arch. Pathol. Lab. Med.* **1998**, *122*, 182–186.
- (6) Philippova, T. M.; Novoselov, V. I.; Alekseev, S. I. *Bioelectromagnetics* **1994**, *15*, 183–192.
- (7) Van Triest, B.; Loftus, B. M.; Pinedo, H. M.; Backus, H. H. J.; Schoenmakers, P.; Telleman, F.; Tadema, T.; Aherne, G. W.; Van Groeningen, C. J.; Zoetmulder, F. A. N.; Taal, B. G.; Johnston, P. G.; Peters, G. J. *J. Histochem. Cytochem.* **2000**, *48*, 755–760.
- (8) Rhodes, A.; Jasani, B.; Balaton, A. J.; Barnes, D. M.; Anderson, E.; Bobrow, L. G.; Miller, K. D. *Am. J. Clin. Pathol.* **2001**, *115*, 44–58.
- (9) Bismuto, E.; Mancinelli, F.; d’Ambrosio, G.; Massa, R. *Eur. Biophys. J. Biophys. Lett.* **2003**, *32*, 628–634.

- (10) Roy, I.; Gupta, M. N. *Curr. Sci.* **2003**, *85*, 1685–1693.
- (11) Porcelli, M.; Cacciapuoti, G.; Fusco, S.; Massa, R.; d’Ambrosio, G.; Bertoldo, C.; DeRosa, M.; Zappia, V. *FEBS Lett.* **1997**, *402*, 102–106.
- (12) Kappe, C. O. *Chimia* **2006**, *60*, 308–312.
- (13) Gedye, R.; Smith, F.; Westaway, K.; Ali, H.; Baldisera, L.; Laberge, L.; Rousell, J. *Tetrahedron Lett.* **1986**, *27*, 279–282.
- (14) Previte, M. J. R.; Aslan, K.; Malyn, S.; Geddes, C. D. *J. Fluoresc.* **2006**, *16*, 641–647.
- (15) Previte, M. J. R.; Aslan, K.; Malyn, S.; Geddes, C. D. *Anal. Chem.* **2006**, *78*, 8020–8027.
- (16) Jain, S.; Sharma, S.; Gupta, M. N. *Anal. Biochem.* **2002**, *311*, 84–86.
- (17) Aslan, K.; Malyn, S. N.; Geddes, C. D. *J. Am. Chem. Soc.* **2006**, *128*, 13372–13373.

With the rapid rise of MAOS and the more recent demonstrations of the applicability of microwaves to aid enzymatically assisted reactions, inexpensive microwave technologies that provide spatially and temporally controlled microwave irradiation are needed.<sup>18</sup> Using finite difference time domain (FDTD) simulation software to solve Maxwell's equations for the interaction of simulated microwave field sources with geometric structures of different dielectric properties, we design aluminum geometric structures to spatially and temporally control the heating and subsequent acceleration of chemically and enzymatically driven reactions. We demonstrate that this technology can locally accelerate chemical reactions to achieve >500-fold increases in "on-demand" photon flux from chemically catalyzed 6- $\mu$ L chemiluminescent reactions.<sup>14,15,17</sup> To demonstrate the clinical and biological relevance of this technology platform, we also report increases in photon flux for chemiluminescent assays on disposable coverslips functionalized with HRP and placed proximal to corners or apexes of aluminum planar structures. We also show that we can locally accelerate chemical reactions and achieve comparable on-demand photon flux from common sensing substrates: such as glass, paper, nitrocellulose, and plastic using disposable aluminum structures. To demonstrate the clinical and biological importance of disposable structures, we affix these aluminum structures in proximity to HRP protein immobilized on nitrocellulose to improve the sensitivity of this Western blot scheme by 50-fold. Finally, we show that this technology can be implemented to develop multiplexed or high-throughput chemiluminescent assays. This promising new, inexpensive microwave technology may prove beneficial across many scientific disciplines, most notably, organic synthesis,<sup>2,3,19–21</sup> enhancing rates of enzymatic reactions,<sup>4,9,10,14,15,17</sup> medicine,<sup>22–24</sup> bioanalysis,<sup>1,10,14,15</sup> and clinical sensing<sup>4,16</sup> to name just a few.

## EXPERIMENTAL SECTION

**Materials.** Bovine-biotinamidocaproyl-labeled albumin (biotinylated BSA), HRP-labeled avidin, 99.999% aluminum evaporation slugs, and premium quality APS-coated glass slides (75  $\times$  25 mm) were obtained from Sigma-Aldrich. CoverWell imaging chamber gaskets with adhesive (2.5 mm diameter, 2 mm deep and 5 mm diameter, 2 mm deep for temperature measurements) were obtained from Molecular Probes (Eugene, OR). Steptavidin–HRP prediluted solution (Catalog No. 20774) was obtained from Chemicon International Inc. Chemiluminescence reagents for these experiments were purchased from Amersham Biosciences (ECL Plus Western blotting detection kit, RPN2132).

**Chemiluminescence Reagents (Chemical Reaction Assays).** The commercially available glow sticks contain the necessary reacting chemicals, which are enclosed within a plastic tube, and yield a bright chemiluminescent emission when they are physically altered. The plastic tube contains a phenyl oxalate ester, a fluorescent probe, and a glass capsule containing the activating

agent (hydrogen peroxide).<sup>25</sup> Activation of the chemicals is accomplished with a bend, a snap, and a vigorous shake of the plastic tube which breaks the glass capsule containing the peroxide and mixes the chemicals to begin the chemiluminescence reaction. Commercially available chemiluminescence materials were purchased and used to demonstrate the utility of the inexpensive microwave reactors.

**Chemiluminescence Reagents (HRP Assay).** The ECL Western Blotting Detection Kit contained two solutions of reacting chemicals that yield a bright chemiluminescent emission at 430 nm upon mixing. Solutions were mixed as described in our previous reports.<sup>14,15</sup>

**FDTD Software and Computation.** FDTD software was purchased from Lumerical Solutions, Inc., to solve Maxwell's equations for structures that have complex geometries or widely varying electromagnetic material properties for a wide variety of microwave field sources. With this software package, we can record time domain information at any spatial point (or group of points) and the frequency domain information at any point (or group of points). Simulations were run on a Dell 690 workstation that is equipped with two 2.66-GHz, 64-bit Dual-Core Intel Xeon 5150 series processors for a total of four execution cores in two sockets and 8 GB of RAM.

**Methods. FDTD Simulations and Theory.** FDTD simulation details are described in detail in the Supporting Information.

**Preparation of Glass Substrates Modified with Thin-Film Aluminum Triangles.** Triangle masks were prepared by cutting shapes 12.3-mm equilateral triangles in aluminum sheets  $\sim$ 100  $\mu$ m thick with the appropriate geometry; i.e., "bow-tie" masks were prepared by removing two 12.3-mm triangle pieces of aluminum such that the triangle tips are separated by a 1-mm distance. Single triangles masks were prepared in a similar fashion. Silanized glass slides were wrapped with aluminum foil masks such that 75-nm aluminum films were deposited on the exposed area of the silanized glass slides by vapor deposition with BOC Edwards Auto 306 instrument. Upon completion, masks were removed and slides modified with aluminum triangle substrates were cut into  $\sim$ 1  $\times$  1.5 in<sup>2</sup> rectangles.

**Preparation of Glass, Paper, Plastic, and Nitrocellulose (NC) Substrates Modified with Thin-Film Aluminum Triangles.** Equilateral 12.3-mm triangle and 8-mm square geometries were constructed by cutting structures with a stencil and blade. Triangle or square pieces of aluminum sheets were affixed to glass, plastic, paper, and nitrocellulose substrate with the same geometry, 1.5 cm  $\times$  1 cm. Disjointed bow-tie geometries were constructed from two inverted 12.3-mm triangles, such that the distance between the apexes or gap size was  $\sim$ 1 mm. Image wells were placed at the corners of the square geometries, at the center of the square geometries, at the tip of a single aluminum triangle, between two aluminum triangles, at the center of the aluminum triangle, and on the plain glass substrates and were subsequently filled with 6  $\mu$ L of blue chemiluminescence material. Photographs of the sample geometries were taken before and after the application of low-power microwave pulses and intensity counts were subsequently collected for 150 s at 100-ms time intervals.

(18) Adam, D. *Nature* **2003**, *421*, 571–572.

(19) Kappe, C. O. *Curr. Opin. Chem. Biol.* **2002**, *6*, 314–320.

(20) Sridar, V. *Curr. Sci.* **1998**, *74*, 446–450.

(21) Whittaker, A. G.; Mingos, D. M. P. *J. Chem. Soc., Dalton Trans.* **1995**, *12*, 2073–2079.

(22) Lin, J. C. *IEEE Trans. Microwave Theory Tech.* **1986**, *34*, 481–483.

(23) Arber, S. L.; Lin, J. C. *Bioelectromagnetics* **1985**, *6*, 257–270.

(24) Lin, J. C.; Yuan, P. M. K.; Jung, D. T. *Bioelectrochem. Bioenerg.* **1998**, *47*, 259–264.

(25) Catherall, C. L. R.; Palmer, T. F.; Cundall, R. B. *J. Chem. Soc., Faraday Trans. I* **1984**, *80*, 823–836.

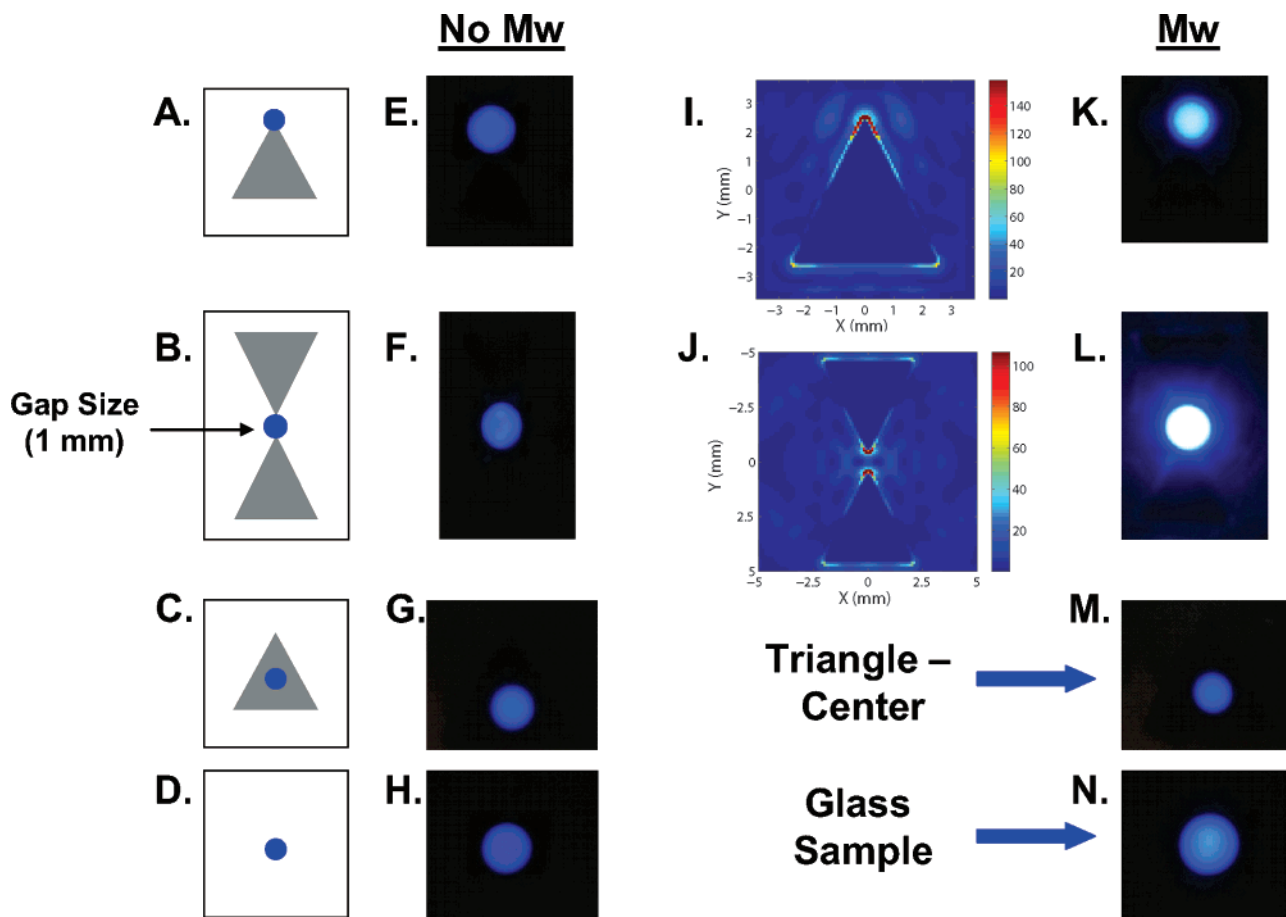


**Figure 1.** (A–D) Sample geometry depicting the chemiluminescence sample (blue circle), glass substrate (white square), and aluminum triangle geometries (12.3-mm length; 1-mm gap size for disjointed bow-tie geometry). (E–H) Before the application of a low-power microwave pulse (no Mw), the chemiluminescence signal is approximately equivalent for all sample geometries. (I, J) Simulated intensity ( $I_x + I_y$ ) images for a TE polarized 2.45-GHz total field scattered field source incident upon a 3D 12.3-mm equilateral triangle (left) and 3D disjointed bow-tie geometry with a gap size (arrow) of 1 mm (right) 100  $\mu\text{m}$  thick. The images shown are a  $xy$  plane cross section of the middle of the 3D simulated structure ( $z = 0 \mu\text{m}$ ). (K–N) Upon application of low-power, 2.45-GHz microwave pulses (Mw), the experimental localized signal enhancement (triggered chemiluminescence) is shown.

**Chemiluminescence Reaction Assays.** Upon activation of chemical reaction, 6  $\mu\text{L}$  of solution placed in the imaging chambers affixed to the plain glass substrate (Figure 2A–D). Following addition of the chemicals to the imaging chambers, each sample was subsequently placed in the microwave cavity and signal intensity was monitored for  $\sim 50$  s. The samples were then exposed to a 5-s low-power microwave pulse (10% power), and the signal was again monitored for the duration of the pulse and a total of 50 s before the application of a second pulse. In total, three 5-s pulses were applied to the respective sample geometries at 50-s time intervals, and the signal intensity was measured at 100-ms intervals for 200 s. For coverslip detection, the experimental and detection conditions are repeated with the same procedure outlined above with the exception of the modified sample geometry (Figure 3A).

Reaction progress for chemiluminescent solutions on different sample geometries is determined by measuring intensity signal at 100-ms time intervals, and results are plotted as  $I_0/I$  ratios versus time (seconds), where  $I_0$  is the intensity before microwave pulsing and  $I$  is the intensity during pulsing. Data are fit to single-exponential decays ( $e^{-kt}$ ) and fits are shown as solid lines. The average of two experimental values is plotted with the difference shown by error bars.

**Temperature Measurements and Arrhenius Plots.** In order to estimate the relative temperature increases of the solutions on the surfaces with different sample geometries, an Arrhenius curve calibration was performed with preheated chemiluminescent solution. Chemiluminescent dye solution was heated in a boiling water bath, and 50  $\mu\text{L}$  was subsequently removed from the heated solution and placed in an image chamber well on a preheated microscope slide. Intensity measurements were made and plotted with the corresponding sample temperatures that were measured with a temperature probe. The natural logarithm of the intensity was plotted versus the inverse of the temperature measurements and fit to the Arrhenius equations (inset, Figure 2B) using Matlab's nonlinear least-squares optimization routine (inset, Figure 2B). Using the resultant fitting equation, further points were extrapolated to determine the relative corresponding temperatures for higher intensity values (dashed extension line, Figure 2B). Normalized intensities for microwave measurements were corrected according to precalibrated room-temperature data ( $I_{19.40^\circ}/I_0 = .90$ ).

**Ru(by)<sub>2</sub>Cl<sub>2</sub> Temperature Measurements.** In order to estimate the relative temperature increases of the solutions on the surfaces with different sample geometries, the intensity of fluorescence emission was measured from 0.1  $\mu\text{M}$  aqueous

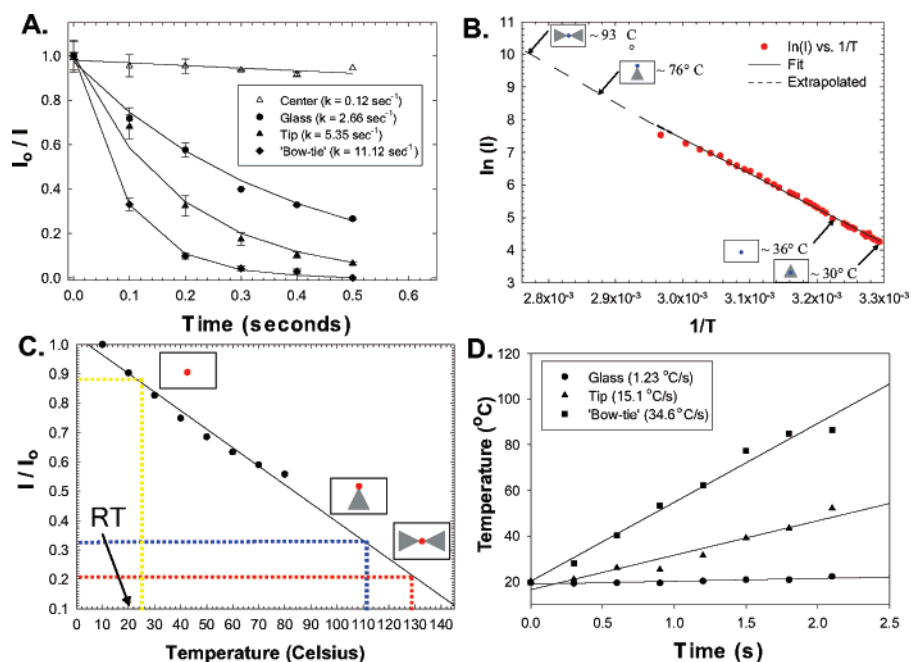


**Figure 2.** (A) Reaction progress for chemiluminescent solutions on different sample geometries plotted as  $I/I_0$  ratios versus time (seconds), where  $I_0$  is the intensity before microwave pulsing and  $I$  is the intensity during pulsing. Data are fit to single-exponential decays ( $e^{-kt}$ ), and fits are shown as solid lines. The average of two experimental values is plotted with the difference shown by error bars. (B) Arrhenius plot and fit for the chemiluminescence reaction on glass slides and the estimated temperature increase for the different sample geometries after exposure to low-power microwave pulses. Sample geometries are shown (insets). (C) Upon application of 5-s, low-power, 2.45-GHz microwave pulses, the subsequent decrease in  $\text{Ru}(\text{by})_2\text{Cl}_2$  sample emission intensity ( $I$ ) was measured and normalized with respect to the pre-Mw pulse intensity ( $I_0$ ). Subsequently, the temperature values are determined from a precalibrated intensity vs temperature plot of a  $\text{Ru}(\text{by})_2\text{Cl}_2$  sample of the same concentration. Room temperature (RT) is noted and sample geometries are shown (insets). (D) Heating rates for  $\text{Ru}(\text{by})_2\text{Cl}_2$  solutions on different sample geometries are plotted as temperature ( $^\circ\text{C}$ ) versus time (seconds). Data are linearly fit according to  $T = (dT/dt)\tau + 1$ , and fits are shown as solid lines. The average of two experimental values is plotted.

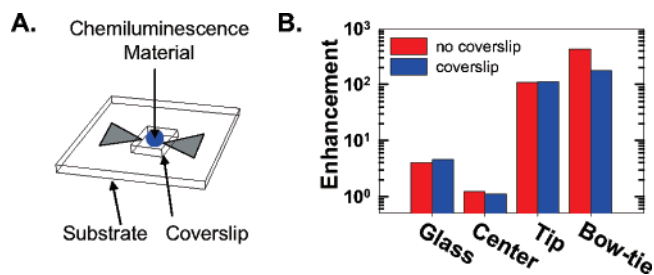


**Figure 3.** (A) Coverslip chemiluminescence reaction geometry scheme. Imaging chambers are affixed to No. 1 coverslips and filled with  $6 \mu\text{L}$  of chemiluminescent material (blue circle). Coverslips are positioned on plain glass substrates and glass substrates modified with aluminum triangle (12.3-mm length; 75 nm thick; 1 mm-gap size for two triangles geometry) geometries (insets, middle). (B) Enhancement is calculated from the ratio of chemiluminescence.

solutions of  $\text{Ru}(\text{by})_2\text{Cl}_2$  on glass substrates in the presence and absence of the planar metallic single triangle and bow-tie geometries.<sup>26</sup>  $\text{Ru}(\text{by})_2\text{Cl}_2$  aqueous solutions were excited with a 473-nm laser source, and the resulting emission intensity was monitored at 300-ms time intervals. Upon application of a 5-s, low-power, 2.45-GHz microwave pulses, the maximum decrease in fluorescence intensity from the  $\text{Ru}(\text{by})_2\text{Cl}_2$  aqueous solutions was recorded and normalized with respect to the room temperature (pre-Mw pulse) emission intensity. Subsequently, the corresponding temperature values were determined from a precalibrated

intensity versus temperature plot of a  $\text{Ru}(\text{by})_2\text{Cl}_2$  sample of the same concentration using a Cary Eclipse fluorescence spectrometer with temperature controller. Calibration temperatures were 10, 20, 30, 40, 50, 60, and  $70 \text{ }^\circ\text{C}$ . Heating rates for  $\text{Ru}(\text{by})_2\text{Cl}_2$  samples on different sample geometries were determined by measuring fluorescent intensity from solutions at 300-ms time intervals. Data are corrected for room-temperature measurements from precalibrated  $\text{Ru}(\text{by})_2\text{Cl}_2$  intensity data. Data are linearly fit according to  $T = (dT/dt)\tau + 1$  using Matlab's nonlinear least-squares optimization routine, and fits are shown as solid lines. The average of two experimental values is plotted (Figure 2C, D).

**Preparation of the Model Protein Assay (Biotin–Streptavidin) on Glass Coverslips.** The model assay used in this paper is based on the well-known interactions of biotin and avidin. Biotin groups are introduced to the glass coverslips (No. 1) through biotinylated BSA, which readily forms a monolayer on the surfaces of glass.<sup>27–29</sup> Glass coverslips were cleaned with dilute solutions of detergent, soaked in concentrated nitric acid, rinsed with deionized, distilled water, and plasma cleaned for 30 s. Coverslips were incubated with  $50 \mu\text{L}$  of  $1 \mu\text{M}$  biotinylated BSA solutions for  $\sim 1$  h. Coverslips were washed with water to remove the unbound material. Coverslips were then incubated with  $50 \mu\text{L}$  of 1.5% aqueous BSA (w/v) for 1 h to minimize nonspecific binding

(27) Green, N. M. *Adv. Protein Chem.* **1975**, *29*, 85–133.

(28) Wilchek, M.; Bayer, E. A. *Anal. Biochem.* **1988**, *171*, 1–32.

(29) Wilchek, M.; Bayer, E. A. *Methods Enzymol.* **1990**, *184*, 14–45.

(26) Filevich, O.; Etchenique, R. *Anal. Chem.* **2006**, *78*, 7499–7503.

of HRP–streptavidin to surfaces. Coverslips were again washed with water to remove excess BSA blocking solution. BSA–biotin functionalized coverslips were incubated with 50  $\mu\text{L}$  of 1  $\mu\text{M}$  HRP–streptavidin and were typically microwaved for 20 s in the microwave cavity (0.7 ft<sup>3</sup>, GE compact microwave model JES735BF, maximum power 700 W). Control coverslips were incubated with only 1.5% BSA solutions and subsequently incubated with 50  $\mu\text{L}$  of 1  $\mu\text{M}$  HRP–streptavidin and exposed to low-power microwave pulsing for 20 s.<sup>30</sup> In all the experiments performed with low-power microwaves, there was no evidence of surface drying. Following incubation, imaging chambers were again washed with water to remove unbound HRP–streptavidin material prior to the chemiluminescence experiments. Imaging chambers were then affixed over incubation area prior to the addition of chemiluminescence experiments.

**Chemiluminescence from Reagents on HRP-Functionalized Glass Coverslips.** In order to obtain the same initial chemiluminescence emission for all measurements, all chemiluminescent assays were undertaken by combining 40  $\mu\text{L}$  of solution A (peroxide mixture from ECL Plus Detection Kit Reagents) with 2.0  $\mu\text{L}$  of solution B (acridan mixture from ECL Plus Detection Kit Reagents), incubated for 5 min, and then added to the imaging chambers. The final sample geometry is the HRP-functionalized coverslip with an imaging chamber filled with chemiluminescence solution. The coverslip is then placed on the top of glass substrates, whereby the center of the imaging chamber is positioned proximal to triangle structures, if present. (see sample geometry, Figure 3A). Data collection commenced immediately following the addition of the reagents to the imaging chambers. The chemiluminescence signal was over 1-s discrete time intervals for 350 s before, during, and after microwave heating inside the microwave cavity (0.7 ft<sup>3</sup>, GE compact microwave model JES735BF, maximum power 700 W). Microwave acceleration was achieved by applying four 10-s microwave pulses at 50-s time intervals. Data collection was terminated after 350 s.

**Chemiluminescence Reaction Assays from Glass, Paper, Plastic, and Nitrocellulose Substrates Modified with Disposable Aluminum Triangle Structures.** Upon activation of chemical reaction, 6  $\mu\text{L}$  of solution was added to the imaging chambers affixed to respective positions in proximity to single aluminum triangle, bow-tie, or square structures (Figure 1, far left). Following addition of the chemicals to the imaging chambers, each sample was subsequently placed in the microwave cavity and signal intensity was monitored for  $\sim$ 150 s. For all chemically induced chemiluminescent experiments, glass, plastic, paper, and NC substrates were cut into equal-sized samples to minimize variations of the convective microwave heating that may arise due to variations in the size of the glass substrates. The samples were exposed to a 5-s, low-power microwave pulse (10% power), and the signal was again monitored for the duration of the pulse and a total of 50 s before the application of a second pulse. In total, three 5-s pulses were applied to the respective sample geometries at 50-s time intervals, and the signal intensity was measured at 100-ms intervals for 200 s. Reported intensity measurements represent the mean of the maximum intensity values recorded during the application of the microwave pulse.

For multiplexed assay experiments, 6- $\mu\text{L}$  samples of four different colored chemiluminescent (green, red, blue, yellow) solutions were placed at the corners of an 8-mm aluminum foil square affixed to a glass substrate (Figure 7). Prior to the application of a low-power microwave pulse, we observed similar luminescent intensities from the four samples. Upon the application of a 5-s, low-power microwave pulse (70 W), we observed similar enhancements from the four chemiluminescent solutions at the corners of the aluminum square.

**Preparation of the Model Protein Assay on Nitrocellulose Membranes.** PVDF membranes were obtained from Biorad and are considered a suitable substrate substitute for NC membranes.<sup>31</sup> Membranes were cut into 1-cm squares and were immersed in 100% methanol for a few seconds until translucent. Membranes were transferred to transfer buffer and incubated until equilibrated (2–3 min). Ten microliters of HRP dilutions was spotted on the center of the membrane to yield an approximately 100 ng, 10 ng, 1 ng, and 200 pg of protein. Control samples were prepared by spotting 10  $\mu\text{L}$  of transfer buffer onto the membrane. Upon spotting the protein to the membranes, membranes were allowed to dry to completion. Round imaging chambers ( $\sim$ 2 cm round) were affixed to glass slides, and dried membrane was placed at the center of the chamber.

**Chemiluminescence from Reagents on Nitrocellulose Membranes with Immobilized HRP.** In order to obtain the same initial chemiluminescence emission for all measurements, all nitrocellulose chemiluminescent assays were undertaken by combining 80  $\mu\text{L}$  of solution A (peroxide mixture from ECL Plus Detection Kit Reagents) with 2.0  $\mu\text{L}$  of solution B (acridan mixture from ECL Plus Detection Kit Reagents), added to the imaging chambers, and incubated for 5 min. For membranes modified with triangle geometries, 12.3-mm aluminum foil triangle structures were affixed to the membrane at the perimeter of the HRP-spotted regions. Data collection commenced immediately following the addition of the reagents to the imaging chambers. The chemiluminescence signal was collected over 1-s discrete time intervals for 50 s before, during, and after microwave heating inside the microwave cavity (0.7 ft<sup>3</sup>, GE compact microwave mode JES735BF, maximum power 700 W). Microwave acceleration was achieved by applying three 10-s microwave pulses at 50-s time intervals. Pulses were applied at 10% power. Data collection was terminated after 200 s.

**Chemiluminescence Detection.** Chemiluminescence spectra were collected using an Ocean Optics spectrometer, model HD 2000 (Dunedin, FL), connected to an Ocean Optics 1000- $\mu\text{m}$ -diameter fiber with an NA of 0.22. The fiber was positioned vertically on top of the slides containing the chemiluminescent reagents inside the microwave cavity. Chemiluminescent spectra and time-dependent emission intensities were collected with an integration time of 100 ms for  $\sim$ 200 s unless otherwise noted. For reactions performed directly on substrate surfaces (no coverslips, Figure 1), signal intensities from reaction substrates with triangle, and bow-tie geometries were collected in the presence of a neutral density filter (ND 0.9). Resultant intensity values displayed in Table 1 for these two geometries were appropriately scaled (multiplication factor of  $\sim$ 8) to facilitate the

(30) Aslan, K.; Geddes, C. D. *J. Fluoresc.* **2006**, *16*, 3–8.

(31) Chen, L. M.; Liang, Y.; Tai, J. H.; Chern, Y. J. *Biotechniques* **1994**, *16*, 600–601.

**Table 1. Tabulated Intensities before and after Microwave Exposure and Subsequent Enhancements for Chemiluminescent Solutions on Glass, Paper, Nitrocellulose (NC), and Plastic Substrates Modified with Square, Triangle, or Disjointed “Bow-Tie” Sample Geometries<sup>a</sup>**

Substrate	Glass	Plastic	NC	Paper
no structure control	3.4 (40, 135)	5.2 (72, 377)	5.6 (37, 209)	8.7 (80, 700)
triangle, center	1.4 (47, 68)	1.14 (87, 100)	1.5 (34, 53)	1.4 (77, 110)
triangle, tip	120 (58, 6925)	256 (59, 15317)	260 (38, 9760)	81 (81, 6440)
triangle, 2 tips	571 (50, 28970)	580 (59, 34190)	447 (56, 20230)	395 (80, 31453)
square, center	1.4 (101, 116)			
square, corner	327 (107, 35000)			

<sup>a</sup> The first number is the enhancement factor; the numbers in parentheses are counts; no Mw, counts Mw.

direct comparisons of intensity measurements for all sample geometries. Integration time was kept constant between the control and silver island film sample measurements.

The real-color photographs were taken with an Olympus digital camera (C-740, 3.2 Mega Pixel, 10× Optical Zoom) without the need for optical filters.

## RESULTS

**Microwave “Triggered” Chemiluminescence.** To design small inexpensive microwave structures that locally accelerate chemical reactions, we used FDTD simulation software to visualize electric field distributions for aluminum structures in a microwave field (Figure 1I, J). We determined that the electric field distributions for a single aluminum 12.3-mm triangle structure (Figure 1I) 100 μm thick (approximate thickness of the disposable aluminum structures described above) in a simulated 2.45-GHz total field scattered field (TFSF) that propagates from left to right. For a 2D cross section at the middle of the 3D structure (at  $z = 0$  μm), intense field enhancements are observed proximal to the tips of the triangles and the maximum enhancement is observed at the triangle’s apex (Figure 1I). Due to their simple design and single point focused electric field enhancements, bow-tie antenna geometries (two triangle geometries that are mirror images and joined at the apex) are commonly implemented to receive radio frequency transmissions.<sup>32</sup> We adapted this concept to design a disjointed bow-tie configuration, such that the two triangles are separated by a gap distance,  $D$ , of 1 mm (Figure 1B). With this configuration, we in theory short circuit the propagation of the 2.45-GHz microwave field (TFSF, TE-polarized) across the metal surface, such that charge builds up in the gap of the bow-tie. The electric field intensity distribution ( $E_x^2 + E_y^2$ ) of a 2D cross section (at  $z = 0$  μm) for the disjointed bow-tie geometry with a 1-mm gap size is shown (Figure 1J). With this configuration, we observed that the maximum field enhancement was localized at the gap between the two triangles. While additional gap sizes were simulated, 1-mm gap sizes were found to provide convergent solutions and substantial field enhancements, which diminish for larger gap sizes and lead to dielectric breakdown for smaller gaps (Supporting Information, Figures S-1 and S-2).

In order to demonstrate that regions of maximum field enhancements for triangle and disjointed bow-tie geometries spatially correlate with regions of maximum chemiluminescent enhancements, we vapor deposited 12.3-mm aluminum triangles

75 nm thick onto silanized glass microscope slides. For two triangle substrates, the gap sizes were set to be ~1 mm. Glass and aluminum triangle-modified substrates were cut into equal sized samples to minimize variations of the convective microwave heating that may arise from variations in the size of the glass substrates. For bow-tie and triangle structures, image wells were affixed to the substrates, such that the tip of single triangle and junction of the bow-tie geometry were exposed to the solution in the well (Figure 1A, B). Wells on the respective sample geometries were subsequently filled with 6 μL of blue chemiluminescence material (Figure 1A–D, blue circles). Photographs of each of the sample geometries before the application of low-power microwave pulses were taken and show that the pre-microwave intensities for each of the samples are approximately equivalent (Figure 1E–H). Samples were subsequently exposed to a short, low-power microwave pulse, and photographs of each of the sample geometries after the application of low-power microwave pulses were taken (Figure 1K–N). The spatial profile of the resultant chemiluminescent signal enhancements for the glass substrates modified with Al geometries (Figure 1K–N) correlate with regions of maximum field enhancements for simulated structures (Figure 1I, J). For glass surfaces modified with the aluminum triangle substrates, we observed >100-fold enhancement in “on-demand” photon flux for the single triangle geometry (Table 1) and >500-fold enhancement for the bow-tie geometry (Table 1). For the chemiluminescence solution placed at the center of the triangle, we observed almost no enhancement in on-demand photon flux (Table 1), which is consistent with the absence of any electric field distribution in the simulated images at the center of the one triangle geometry (Figure 1I). Since the signal intensities for all samples prior to microwave exposure are approximately equivalent (Figure 1E–H, Table 1), it is important to note that this lack of signal enhancement is not due to the quenching of the chemiluminescence emission. Furthermore, spectral shifts in chromophore emission are not observed after exposure to microwave pulses. Thus, we concluded that the reported observations of intensity enhancements are not due to unsuspected changes in photophysical properties, including the destruction of the chromophores (data not shown).<sup>33</sup>

**Reaction Rates.** To determine the corresponding increases in reaction rates of the chemiluminescent reactions during microwave pulsing for the different sample geometries, the inverse

(32) Compton, R. C.; McPhedran, R. C.; Popovic, Z.; Rebeiz, G. M.; Tong, P. P.; Rutledge, D. B. *IEEE Trans. Antennas Propagation* **1987**, *35*, 622–631.

(33) Nemkovich, N. A.; Rubinov, A. N.; Tomin, A. T. In *Topics in Fluorescence Spectroscopy, Vol. 2, Principles*; Lakowicz, J. R., Ed.; Plenum Press: New York, 1991; Vol. 2, pp 367–428.

normalized intensities of the chemiluminescent solutions were plotted as a function of time. During the application of low-power, 5-s microwave pulses, we measured the signal intensities at 100-ms time intervals. Since intensity indicates the extent of reaction progress, we plotted  $I_0/I$  versus time, where  $I_0$  is the intensity before microwave pulsing and  $I$  is the intensity during pulsing (Figure 2A). The curves are fit to single-exponential decays ( $I_0/I = e^{-kt}$ ) using a least-squares fitting algorithm to determine the reaction decay rates for the different sample geometries. While the reaction rates on the center of the triangle structures are indicative of the steady-state decays for chemiluminescent solutions at room temperature ( $0.12 \text{ s}^{-1}$ ), we report a 20-fold enhancement for microwave-triggered chemiluminescent reaction rates on glass substrates ( $2.66 \text{ s}^{-1}$ ). In the presence of the aluminum structures, we report 45- and 95-fold enhancements for chemiluminescent reaction rates for the single triangle ( $5.35 \text{ s}^{-1}$ ) and bow-tie geometries ( $11.12 \text{ s}^{-1}$ ), respectively (Figure 2A).

We also recorded the reaction decay rates after the application of low-power, 5-s microwave pulses (Supporting Information, Table S1). Reaction decay rates were fit to a multiexponential decay model,  $I(t) = \sum_i A_i e^{-k_i t}$ , where  $k_i$  is the decay rate of component  $i$  and  $A_i$  is its amplitude such that  $\sum_i A_i = 1.0$ . After microwave pulsing, we observed that the amplitude-weighted decay rates,  $\langle k \rangle = \sum_i k_i A_i$ , are increased by >2-fold and almost 3-fold for the chemiluminescence samples at the tips of a single triangle (Supporting Information, Table S1 and Figure S3) and the gap of the disjointed bow-tie geometries (Table S1 and Figure S3), respectively.

**Temperature Effects.** To estimate the relative temperature increases of the chemiluminescent solutions on the surfaces with different sample geometries, an Arrhenius calibration curve was constructed using a preheated chemiluminescent solution.<sup>34</sup> The natural logarithm of the intensity was plotted versus the inverse of the temperature measurements and fit to the Arrhenius equation (inset, Figure 2B). Using the fitting function, further points were extrapolated to determine the relative corresponding temperatures for higher signal intensity values (dashed extension line, Figure 2B). We note that the measured intensity values of these samples correlate with significant temperature increases at the tip of a single aluminum triangle structure ( $76 \text{ }^\circ\text{C}$ , Figure 2B inset) and in the gap of the disjointed bow tie geometry ( $93 \text{ }^\circ\text{C}$ , Figure 2B inset). We also note that the temperature of the glass sample ( $36 \text{ }^\circ\text{C}$ , Figure 2B inset) is higher than the temperature of the sample at the center of the triangle ( $30 \text{ }^\circ\text{C}$ , Figure 2B inset).

To determine the corresponding changes in heating rates and final temperature of aqueous solutions for the different sample geometries, we recorded the intensity of fluorescence emission from aqueous solutions of  $\text{Ru}(\text{by})_2\text{Cl}_2$ .<sup>26</sup> It is well-established that the intensity of the fluorescence emission from an aqueous solution of  $\text{Ru}(\text{by})_2\text{Cl}_2$  is inversely proportional to the temperature of the solution. From precalibrated normalized intensity versus temperature plot of a  $\text{Ru}(\text{by})_2\text{Cl}_2$  sample of the same concentration that was fit to a linear function,  $I/I_0 = (dI/dT)T + 1$ , where  $I_0$  is the intensity before microwave pulsing and  $I$  is the intensity during pulsing (Figure 2C).

From these results, we calculated the corresponding temperature increases for the different sample geometries at discrete time points to determine the relative heating rates (Figure 2D).

In the absence of the aluminum triangle structures, the heating rate for the  $\text{Ru}(\text{by})_2\text{Cl}_2$  solution on glass was determined to be  $1.23 \text{ }^\circ\text{C/s}$ , which is consistent with previously reported rates for microwave dielectric heating of water.<sup>35</sup> In the presence of a single triangle structure, the heating rate is  $15.1 \text{ }^\circ\text{C/s}$  and the heating rate is more than doubled ( $34.6 \text{ }^\circ\text{C/s}$ ) in the presence of the bow-tie or two-triangle geometry. Although the final calculated temperatures for the triangle ( $\sim 110 \text{ }^\circ\text{C}$ ) and bow-tie ( $130 \text{ }^\circ\text{C}$ ) geometries indicate that the aqueous solutions are superheated,<sup>35</sup> it is important to note that these values are beyond the range of the linear dependence of the emission intensity of  $\text{Ru}(\text{by})_2\text{Cl}_2$  solutions.<sup>36,37</sup> Thus, these values are only rough approximations of the final temperatures.

**Transferable Aluminum Substrates for Disposable Surface Assay Applications.** Since three-dimensional FDTD simulation data of the triangle geometries (Supporting Information, Figures S-4 and S-5) show that the enhanced field also persists in the  $z$  dimension, i.e., vertically, we affixed imaging chambers to No. 1 coverslips (Corning Labware & Equipment) and added  $6 \mu\text{L}$  of chemiluminescent solution. The imaging chamber and solution on top of the coverslip are placed on the top of glass substrates, whereby the center of the imaging chamber is positioned proximal to triangle structures, if present (see sample geometry, Figure 3A). The samples were again exposed to short, low-power microwave pulses. With the coverslip sample geometries (Figure 3A), we observed the same trend for increases in on-demand photon flux that was documented for the reactions that were placed directly on the modified metal substrates (Figure 1K–N). In order to compare signal enhancements for the two sample geometries, we calculated the ratio of the signal after microwave pulsing to signal before microwave pulsing and compared the relative signal enhancement ratios (Figure 3B). We observed that the presence of the coverslip did result in minor signal enhancement loss for the bow-tie geometry ( $\sim 2$ -fold). Although we strived to position the coverslip samples exactly at the center of the triangle tips such that we could best reproduce the position of the samples placed directly on the substrates, it is also possible that some signal loss could be due in part to the variance in position of the coverslip over the triangle tips, as well as the decrease in the electric field intensity above the sample surface (Supporting Information, Figures S-4 and S-5).

With the observation that we could still create signal enhancements on coverslips placed above the sample geometries, we chose to demonstrate the utility of this result. We incubated coverslips with a  $1 \mu\text{M}$  BSA–biotin solution and subsequently incubated the functionalized coverslips with HRP–streptavidin to create a model protein detection assay. We subsequently added acridan/peroxide mixture to the imaging well affixed to the functionalized coverslip to simulate a typical HTS well format. Without microwave heating, a weak, steady “slow glow” chemiluminescent intensity is observed due to the presence of BSA–biotin/HRP–streptavidin complexes (Figure 4A, blue bar). Due to the 1-s integration times and the limited detection sensitivity of our system, the weak signal is characteristic of the photon flux

(34) Bindel, T. H. *J. Chem. Educ.* **1996**, *73*, 356–358.

(35) Baghurst, D. R.; Mingos, D. M. P. *J. Chem. Soc., Chem. Commun.* **1992**, 674–677.

(36) Durham, B.; Caspar, J. V.; Nagle, J. K.; Meyer, T. J. *J. Am. Chem. Soc.* **1982**, *104*, 4803–4810.

(37) Vanhouten, J.; Watts, R. J. *J. Am. Chem. Soc.* **1976**, *98*, 4853–4858.

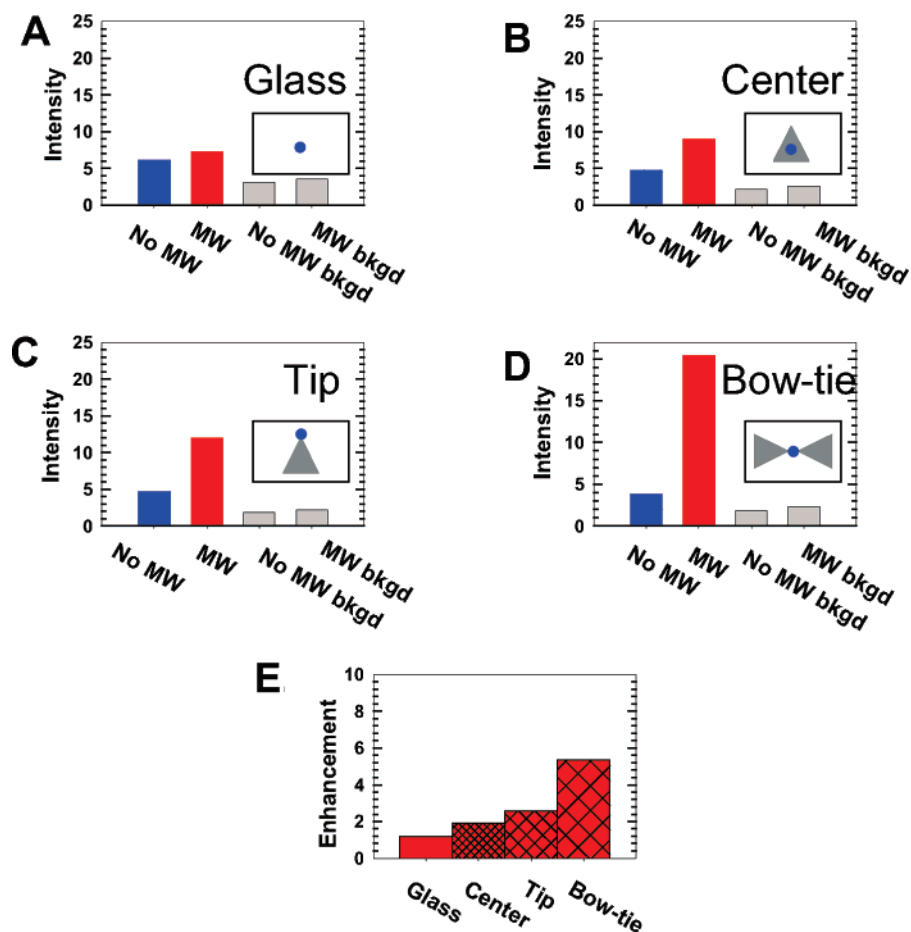


**Figure 4.** (A–D) Chemiluminescence emission before (blue bars) and after (red bars) exposure to low-power microwave (Mw) pulses from glass coverslips incubated with 1  $\mu$ M BSA–biotin and 1  $\mu$ M HRP–streptavidin positioned on glass substrates modified with and without 12.3-cm Al triangle 75 nm thick (top 4 panels). Chemiluminescence emission before and after exposure to low-power microwave (Mw) pulses from control glass coverslips incubated with 1.5% BSA and 1  $\mu$ M HRP–streptavidin (gray bars) (E) Chemiluminescent microwave (Mw) enhancement ratios (Mw/no Mw) upon application of low-power microwave pulses (Mw) for different sample geometries.

from a HRP-triggered chemiluminescent reactions (See Supporting Information, Comment on Detection Sensitivity and Figure S-6). More importantly, similar pre-microwave intensities are observed for the coverslip samples on the different sample geometries (Figure 4A–D, blue bars). Thus, we can deduce that the relative surface HRP concentrations for each of the samples is approximately equivalent and subsequent intensity enhancements are due to the exposure to microwave fields, not varying surface HRP concentrations. In addition, we show that the control samples (surfaces modified with 1.5% BSA and HRP–streptavidin) show no initial intensity counts (Figure 4A–D, gray bars).

To demonstrate the benefits of microwave heating to increase the detected chemiluminescent signal from the surface assays, we monitored the photon flux (in counts), which is the area under the curve of the intensity–time plot (Supporting Information, Figure S-6). The photon flux indicates the extent of the HRP-catalyzed reaction and thus provides information about the presence of surface-bound BSA. The triggered “peaks” seen after each microwave exposure (Supporting Information, Figure S6) are due to the application of the low-power microwave magnetron pulse. During the 10-s microwave exposures, the chemiluminescent intensity is triggered by the magnetron pulsing and the localized heating of the microwaves. It is clear from the signal intensity time traces (Figure S6) and the histogram plots (Figure

4A–D, red bars) that the maximum photon flux was generated from the disjointed bow tie geometry samples (Figure S6; Figure 4D). The microwave pulses were also applied to control samples, and no intensity enhancements are evident in the absence of BSA–biotin/HRP–streptavidin complexes (Figure S6). In comparison to the sample that was placed on the glass substrate alone, we showed not only a significant signal-to-noise benefit from the modified sample substrates but also we showed that we can uniquely locally trigger the chemiluminescence reaction to occur on demand.

**Transferable Triangle Structures To Trigger Chemiluminescence from Common Substrates.** In addition to the possibility of creating transferable aluminum structures for disposable sensing applications, we further demonstrate the feasibility of creating disposable aluminum structures to increase the sensitivity of protein detection on common sensing substrates. We cut 12.3-mm triangle geometries from aluminum sheets ( $\sim$ 100  $\mu$ m thick) and affixed them to different substrates (Figure 5, legend), such that the gap size was  $\sim$ 1 mm for the disjointed bow tie geometry (Figure 1). Image wells were again placed at the tip of a single aluminum triangle, between two aluminum triangles, at the center of the aluminum triangle, and on plain substrates (Figure 5, bottom). Wells on the respective sample geometries were filled with 6  $\mu$ L of blue chemiluminescence material and subsequently

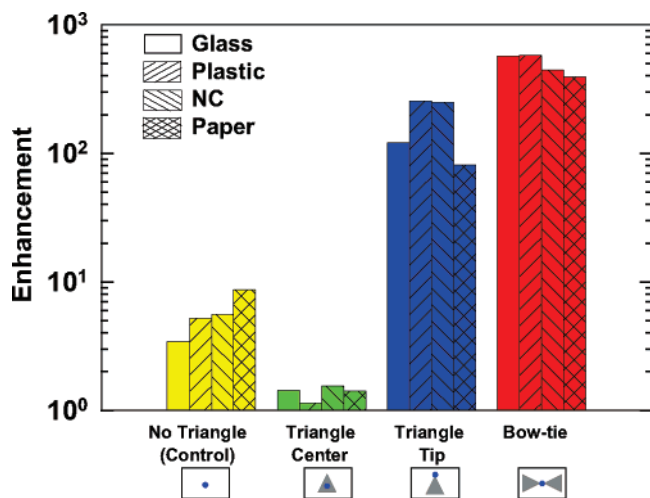


**Figure 5.** Chemiluminescent microwave (Mw) enhancement ratios (Mw/no Mw) upon application of low-power microwave pulses (Mw) for different sample geometries on various dielectric substrates.

exposed to a 5-s microwave pulse. From recorded intensity data, we observed almost equivalent enhancement trends when the technology is adapted to common protein detection sensing substrates, most notably nitrocellulose and plastic (Table 1 and Figure 5).

**Disposable Triangle Structures To Increase Sensitivity of a Model Western Blot Application.** To demonstrate another biologically relevant application of spatially triggered chemiluminescence from a variety of dielectric substrates, we used NC HRP dot blots to model a typical Western blot scheme, whereby proteins are transferred and immobilized on nitrocellulose membranes. The detection limit for our detection scheme without microwave induced enhancement is  $\sim 10$  ng of HRP. With the application of the low-power microwave pulse train, in the absence of aluminum structures, we observed enhancements for 100- and 10-ng samples (Figure 6A, yellow bars), but relatively no enhancement for the 1ng and 200 pg samples (Figure 6A, yellow bars). This is dually noted by a representative emission time traces for the nitrocellulose samples treated with 10 ng of HRP, whereby peaks correspond to microwave (Mw pulse)-induced increases in photon flux (Figure 6B). In the presence of the affixed aluminum triangle, not only do we observe increases in photon flux from the sample (Figure 6B), but also the sensitivity of detection is increased by a factor of 50 (Figure 6A, blue bars). Although we improved detectability of low protein concentrations on nitrocellulose membranes by 50-fold, we believe that we can achieve sensitivity improvements beyond 50-fold with more efficient signal detection means (See Supporting Information, Comment on Detection Sensitivity and Figure S7).

**Multiplexed Chemiluminescent Assay Format.** We also demonstrate that aluminum structures can be implemented to create highly sensitive multiplexed chemiluminescent assays for high-throughput screening with readily available and inexpensive materials. At the corners of the 8-mm square structures  $\sim 100 \mu\text{m}$  thick, the microwave enhancement of the chemiluminescence emission is  $>300$ -fold (Table 1 and Figure 7A). While on a plain glass substrate in the absence of aluminum foil structures, there was only a 3-fold enhancement (Table 1). Thus, the on-demand photon flux at the corners of the aluminum square geometries is

100-fold greater than the on-demand photon flux achieved with conventional microwave heating. For the solution placed on the center of the aluminum structure, we again observed negligible enhancement (1.4-fold) upon exposure to a low-power microwave pulse (Table 1 and Figure 7A). Images of four chemiluminescence solutions of different colors at the corners of 8-mm square aluminum structures are shown before (Figure 7B) and after (Figure 7C) the application of microwave pulses to demonstrate the ability to easily adapt this technology to a multiplexed or high-throughput chemiluminescent assay platform.

## DISCUSSION

Since the simulated aluminum structures are modeled as perfect conductors, maximum spatial field distributions are localized at the corners or tips of the aluminum structures, and "ohmic" loss to the metal and its subsequent heating due to plasmon effects is negligible. As a result, maximum dielectric loss to the solution is proximal to the corners or tips of the aluminum structures. Thus, the increased reaction rates of the chemiluminescent reaction is caused by the subsequent heating of the solution due to dielectric loss, which is also confirmed by Arrhenius plots for the chemiluminescent solutions and increased heating rates and temperatures of the  $\text{Ru}(\text{by})_2\text{Cl}_2$  aqueous solutions.<sup>26</sup> On the other hand, the relative lack of any signal enhancement from the center of the triangle structures confirms a negligible plasmon effect and subsequent ohmic heating on the metal structures. With minimal effort, materials, and equipment, we demonstrate a platform technology to locally trigger chemiluminescent reactions from a variety of dielectric substrates and achieve  $>500$ -fold increases in reactivity.

Since the HRP reactions sustain activity during exposure to microwave pulses and in proximity to the metal structures, the heating of the solution does not deactivate HRP, which suggests other proteins, i.e., alkaline phosphatase, may also be stable under these conditions. While intensely focused microwave fields can lead to uncontrolled temperature increases<sup>38</sup> and, potentially, denature or damage proteins and small molecules, and preclude this technology from being useful for small molecule sensing, this technology affords many practical controls for this effect. The  $>95$ -fold increase in heating rates of aqueous solutions is combined with pronounced cooling of solutions proximal to the conductive metal structures (Supporting Information, Figure S3 and Table S1). Subsequently, this technology potentially offers temperature jumps and rapid cooling rates that exceed denaturation rates of proteins.<sup>39–42</sup> In this regard, it is also conceivable that optimized structures can be designed to adequately balance the heating and cooling rates to develop inexpensive monomode reactors for microwave organic synthesis reactions.<sup>43</sup> Furthermore, the extent of heating can be changed by changing the volume of solution or positioning sample distal from the region of maximum electric

(38) Vriezina, C. A. *J. Appl. Phys.* **1998**, *83*, 438–442.

(39) Rigler, R.; Rabl, C. R.; Jovin, T. M. *Rev. Sci. Instrum.* **1974**, *45*, 580–588.

(40) Kao, J. P. Y.; Tsieng, R. Y. *Biophys. J.* **1988**, *53*, 635–639.

(41) Williams, A. P.; Longfellow, C. E.; Freier, S. M.; Kierzek, R.; Turner, D. H. *Biochemistry* **1989**, *28*, 4283–4291.

(42) Thompson, P. A.; Eaton, W. A.; Hofrichter, J. *Biochemistry* **1997**, *36*, 9200–9210.

(43) Larhed, M.; Wannberg, J.; Hallberg, A. *QSAR Comb. Sci.* **2007**, *26*, 51–68.

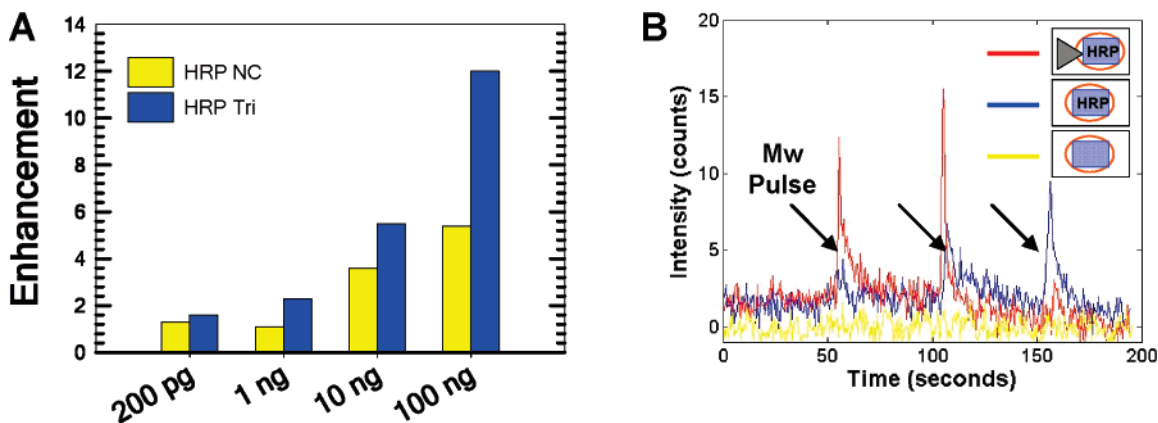


**Figure 6.** (A) HRP assay enhancement as a ratio of maximum chemiluminescent emission to steady-state chemiluminescent emission before application of Mw power HRP assays. Enhancements with (blue bars) and without affixed aluminum foil triangle (yellow bars) are shown. Chemiluminescence signal intensity time traces for (B) 10 ng of HRP on NC membrane samples, whereby 100  $\mu$ L of chemiluminescence solution (acridan/peroxide) was added, and a train of three 5-s microwave pulses (Mw pulse) at 50-s time intervals were applied at low microwave power to induce triggered increases in photon flux. Chemiluminescence signal was recorded for samples with a single affixed aluminum triangle (red trace), no triangle (blue trace), and background signal (no HRP, yellow trace). Sample geometries for HRP immobilized on NC shown in legends (blue squares, NC; gray triangle, Al foil 12.7-mm triangle; orange ring, imaging chamber; and box, glass substrate).

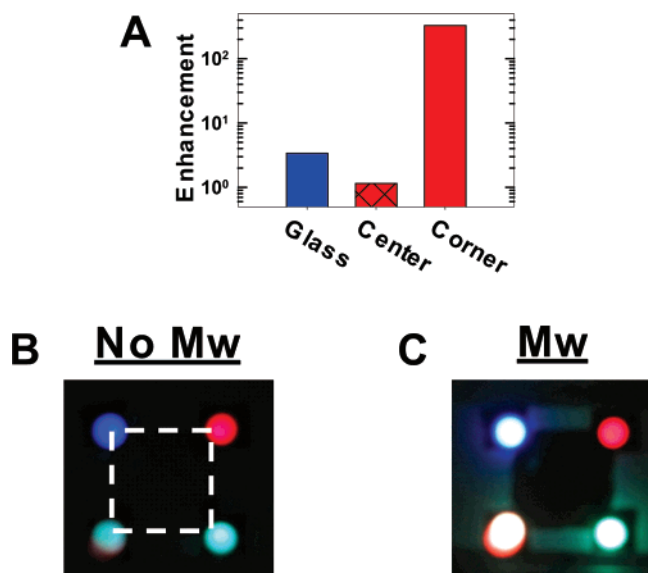


**Figure 7.** (A) Ratio of chemiluminescent intensities after Mw pulses to intensity before Mw pulses for glass (blue bar), the center of the square geometry (hatched red bar), and the corner (solid red bar). (B) Chemiluminescence signal in a multiplexed format is approximately equivalent from all positions on the 8-mm square aluminum foil structure (dashed box) before the application of low-power pulses and (C) significantly enhanced after the application of low-power microwave pulses.

field enhancements. While we have demonstrated the applicability of this technology using 2.45-GHz radiation, preliminary data suggest the general applicability of the technology over a range of microwave frequencies, which implies selective heating of different dielectric media and materials.<sup>44</sup>

The triggering of HRP surface reactions not only provides advantages in terms of signal-to-noise ratios for sensing and biological reactions, but we have observed reduced detection times

for assays performed in the presence of the triangle substrates (Supporting Information, Figure S6). In addition, we showed that disposable planar aluminum structures can be affixed to common sensing substrates, i.e., nitrocellulose membranes, to locally trigger enzyme (HRP)-catalyzed chemiluminescent reactions. We provide a cartoon of a Western blot that demonstrates the potential utility of this technique to amplify weak bands from nitrocellulose membranes by affixing aluminum triangle geometries to regions of interest (Supporting Information, Figure S-7). We suspect that we will see further intensity enhancements with other thin-film geometries, the addition of metal colloids to plasmon enhance luminescence,<sup>45</sup> better characterized assay conditions, and improved detection schemes.

## CONCLUSIONS

We believe that this relatively inexpensive approach to focusing microwave fields can facilitate the general utility of microwave technology in many scientific disciplines. More specifically, we have shown that we can use aluminum geometric substrates to directionally amplify microwave radiation to accelerate solution-based chemical reactions. In addition, we have also shown the potential utility of this generic approach to microwave sensing to provide another means for not only dramatic improvement of signal-to-noise ratios for surface assays but also the potential application of these focused microwaves for the increased specificity, sensitivity, and rapidity of clinical sensing applications, chemical synthesis,<sup>1–3,9,10,14,15,19,20</sup> biological assays,<sup>4,9,10,14,15</sup> biosensing,<sup>3,9,10,14,15</sup> and chemical sensing technologies.<sup>46</sup>

## ACKNOWLEDGMENT

Salary support to authors from UMBI and the IoF is acknowledged.

(44) Mingos, D. M. P.; Baghurst, D. R. *Chem. Soc. Rev.* **1991**, *20*, 1–47.

(45) Previte, M. J. R.; Aslan, K.; Zhang, Y.; Geddes, C. D. J. *Phys. Chem. C* **2007**, *111*, 6051–6059.

(46) Aslan, K.; Geddes, C. D. *Anal. Chem.* **2005**, *77*, 8057–8067.

**SUPPORTING INFORMATION AVAILABLE**

Additional information as noted in text. This material is available free of charge via the Internet at <http://pubs.acs.org>.

Received for review May 21, 2007. Accepted July 10, 2007.

AC071042+

# **Spatial and Temporal Control of Microwave Triggered Chemiluminescence: A Rapid and Sensitive Protein Detection Platform**

*Michael J. R. Previte, Kadir Aslan, and Chris D. Geddes\**

Institute of Fluorescence, Laboratory for Advanced Medical Plasmonics, Medical Biotechnology Center,  
University of Maryland Biotechnology Institute, 725 West Lombard St., Baltimore, MD, 21201.

E-mail: [geddes@umbi.umd.edu](mailto:geddes@umbi.umd.edu)

**Contents:**

<b>FDTD Simulation Supporting Text</b>	<b>S-2</b>
<b>Reaction Rate Decays</b>	<b>S-4</b>
<b>Comment on Detection Sensitivity</b>	<b>S-4</b>
<b>References</b>	<b>S-5</b>
<b>Supporting Table S1</b>	<b>S-6</b>
<b>Supporting Figure S1</b>	<b>S-7</b>
<b>Supporting Figure S2</b>	<b>S-8</b>
<b>Supporting Figure S3</b>	<b>S-9</b>
<b>Supporting Figure S4</b>	<b>S-10</b>
<b>Supporting Figure S5</b>	<b>S-11</b>
<b>Supporting Figure S6</b>	<b>S-12</b>
<b>Supporting Figure S7</b>	<b>S-13</b>

**FDTD (Finite difference Time Domain) Simulation Supporting Text:**

To establish that the spatial distributions of the fields in the xy-plane of the 2D images adequately approximate the spatial field distributions in the xy-plane for convergent three-dimensional simulations of similar structures (Supporting Figures 3 and 4), we performed 3D simulations of the single triangle and disjointed ‘bow-tie’ geometries. To avoid excessive computational times, we decreased the aspect ratio of the triangle geometry such that the equilateral triangle geometries were 5 mm long and 100  $\mu\text{m}$  thick. We insured that the intensities for the images converged by decreasing the mesh size in the xy and z dimensions from .16 mm and .025 mm to .4 mm and .01 mm at three intervals of .04 mm and .005 mm, respectively. Two equilateral 5 mm triangle were modeled by creating a second equilateral triangle structure and aligning its apex with the tip of the mirror triangle, such that the tips are separated by a gap distance, D. Optical properties of triangle structures were defined as perfect

conductors. Thus, the total complex permittivity of a perfect conducting metal, such as aluminum, in the presence of a microwave field is given by

$$\tilde{\epsilon}(f) = \epsilon_{REAL} + i\epsilon_{IMAG} \frac{f_{SIM}}{f} + i \frac{\sigma}{2\pi \cdot f \epsilon_o} \quad (1)$$

where  $\epsilon_{REAL}$  is the real part of the permittivity for the dielectric medium,  $\epsilon_{IMAG}$  is the imaginary of the dielectric medium,  $f_{SIM}$  is the center frequency of all the sources in the simulation,  $f$  is the frequency of the simulation,  $\epsilon_o$  is the permittivity of free space, and  $\sigma$  is the conductivity of the metal.<sup>2</sup> The conductivity value of the metal is approximated to be close to the d.c. value for aluminum,<sup>3</sup>  $3.8 \times 10^7 \text{ Sm}^{-1}$ , the background dielectric media is presumed to be air, and the frequency,  $f$ , is set to 2.45 GHz.

The microwave cavity source used in these experiments was a standard microwave oven that is equipped with a magnetron placed on the outside of the cavity, which is treated with white reflective coating to optimize microwave confinement, standing wave generation, and minimize absorption loss. We modeled this microwave system as a total field scattered electric field (TFSF) to best approximate the electromagnetic field in the microwave cavity during operation and assumed only TE<sub>10</sub> modes could propagate in the microwave cavity.<sup>4</sup> Subsequently, electromagnetic radiation is modeled to propagate from left to right along the x-axis across equilateral triangle(s) structures.

Since we are interested in visualizing the xy spatial field distributions for the chosen planar geometries not the absolute intensities, we also chose to model the planar geometries in two dimensions as an infinite column and ignore the scattering effect in the z-plane. Thus, we show results of 2D FDTD simulations to demonstrate the relative electric field distributions for the planar geometries.<sup>1</sup> While we understand that these simulations will not divulge absolute intensity enhancements, the resultant, normalized field distributions for the simulations are a useful tool to predict the expected field distributions in the xy-plane for our experimental configuration.

For 2D triangle simulations, mesh sizes were set at .1 mm for one triangle and disjointed ‘bow-

tie' simulations. The simulation time is set to 10 ns to insure that the light travels down the surface and back. The absorbing boundary conditions are of the perfectly matched layer type and are used to truncate the FDTD domain in the x and y dimensions.<sup>2</sup> Final images are normalized with respect to the maximum pixel total intensity ( $E_x^2 + E_y^2$ ) for the images.

### Reaction Rate Decays

Reaction rate decay curves for all samples (Figure S3) are collected at a time interval of 100 milliseconds over an approximately 50 second time interval. Reaction decay rates were fit to a multi-exponential decay model,  $I(t) = \sum_i A_i e^{-k_i t}$ , using Matlab's nonlinear least squares optimization routine where  $k_i$  is the decay rate of component  $i$  and  $A_i$  is its amplitude such that  $\sum_i A_i = 1.0$ . The contribution of each component to the steady-state decay rate is given by

$$f_i = \frac{A_i k_i}{\sum_i A_i k_i} \quad (2)$$

the mean decay rate is given by

$$\bar{k} = \sum_i f_i k_i \quad (3)$$

and the amplitude weighted decay rate is given by

$$\langle k \rangle = \sum_i A_i k_i. \quad (4)$$

Reaction decay results for all sample geometries are shown in Table S1.

### Comment on Detection Sensitivity

Since we sought to compare the absolute signal amplification from the sample membranes, we detected the chemiluminescent signal with a 300  $\mu\text{m}$  fiber. Although this detection scheme only affords the collection of less than .2% of the total emitted light, a relative comparison between the standard detection method and 'triggered' methods was still possible.

## References

- (1) Radzevicius, S. J.; Chen, C. C.; Peters, L.; Daniels, J. J. *Journal of Applied Geophysics* **2003**, *52*, 75-91.
- (2) Lumerical Solutions, I. *FDTD Solutions Manual Release 4.0*: Vancouver, BC, 2006.
- (3) Suckling, J. R.; Hibbins, A. P.; Lockyear, M. J.; Preist, T. W.; Sambles, J. R.; Lawrence, C. R. *Physical Review Letters* **2004**, *92*.
- (4) Iwabuchi, K.; Kubota, T.; Kashiwa, T. *Journal of Microwave Power and Electromagnetic Energy* **1996**, *31*, 188-196.

**Supporting Tables:**

<b>Sample:</b>	<b>A<sub>1</sub></b>	<b>k<sub>1</sub> (s<sup>-1</sup>)</b>	<b>A<sub>2</sub></b>	<b>k<sub>2</sub> (s<sup>-1</sup>)</b>	<b>A<sub>3</sub></b>	<b>k<sub>3</sub> (s<sup>-1</sup>)</b>	<b><math>\bar{k}</math></b>	<b><math>\langle k \rangle</math></b>
Glass	0.648	0.35	0.482	9.86×10 <sup>-2</sup>	-	-	0.306	0.274
Al - Center	1.00	4.45×10 <sup>-3</sup>	-	-	-	-	4.45×10 <sup>-3</sup>	4.45×10 <sup>-3</sup>
Al - Tip	0.851	0.73	0.149	3.22×10 <sup>-2</sup>	-	-	0.725	0.626
Al – 2 Tips	0.787	0.86	0.171	0.25	0.0420	2.75×10 <sup>-2</sup>	0.822	0.721

**Table S1:** Chemiluminescence decay rates after 5 second exposure to low power microwaves. All data

fit with  $I(t) = \sum_i A_i e^{-k_i t}$ .

**Supporting Figures:**

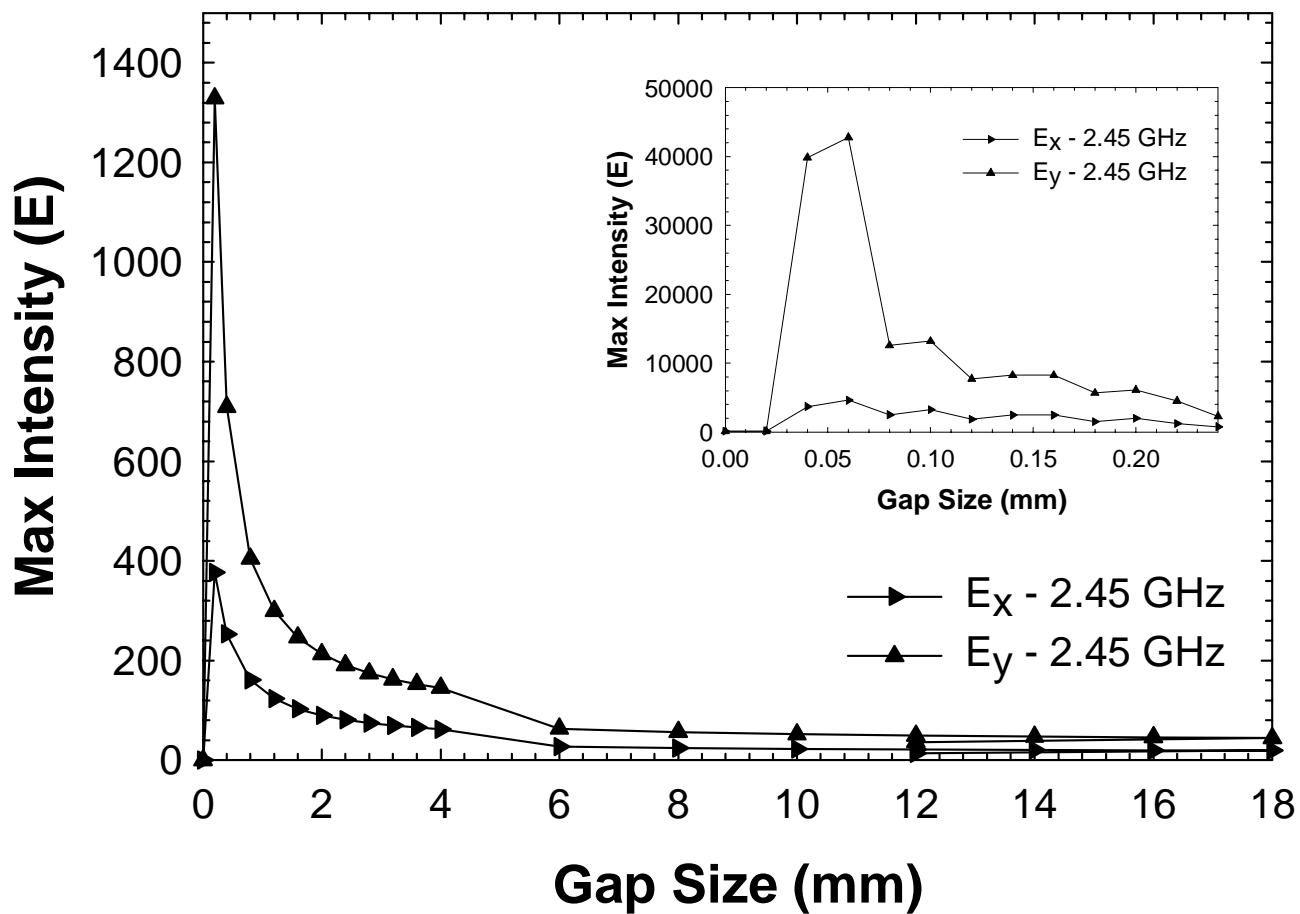


**Figure S1:** Maximum  $I (I_x (E_y^2) + I_y (E_x^2))$  pixel intensity versus gap size for the 2 triangle configurations shown in Supporting Figure 2. Inset, expanded view of maximum pixel intensity versus gap size.

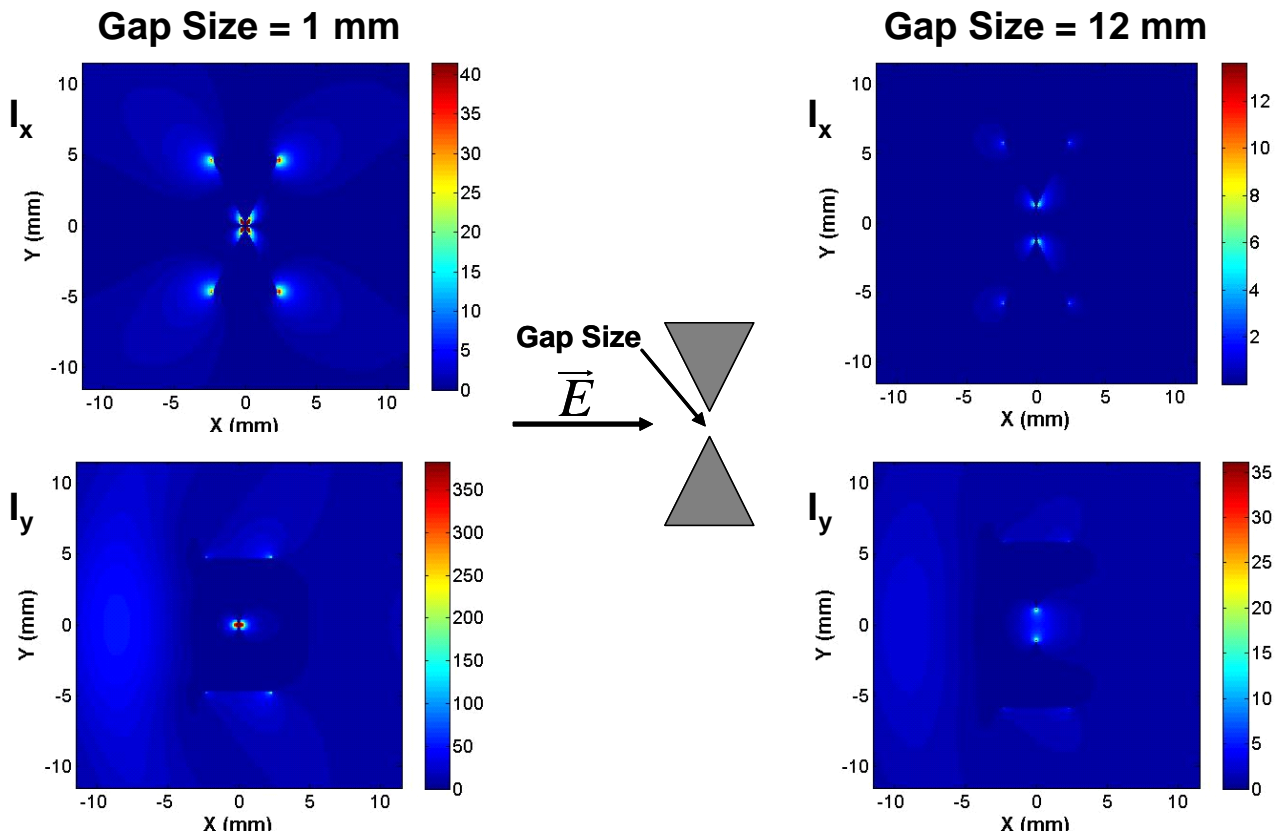


**Figure S2:** Simulated intensity images,  $I_x$  (top) and  $I_y$  (bottom) of the electromagnetic field distribution for 2.45 GHz microwave frequencies incident upon (2) 2-D equilateral triangles with 12.3 mm length and oriented with the sample geometry shown (middle). The incident field is held constant and the gap size is varied in subsequent simulations (Supporting Figure 1), 1 mm (left) and 12 mm (right) gap size examples are shown.

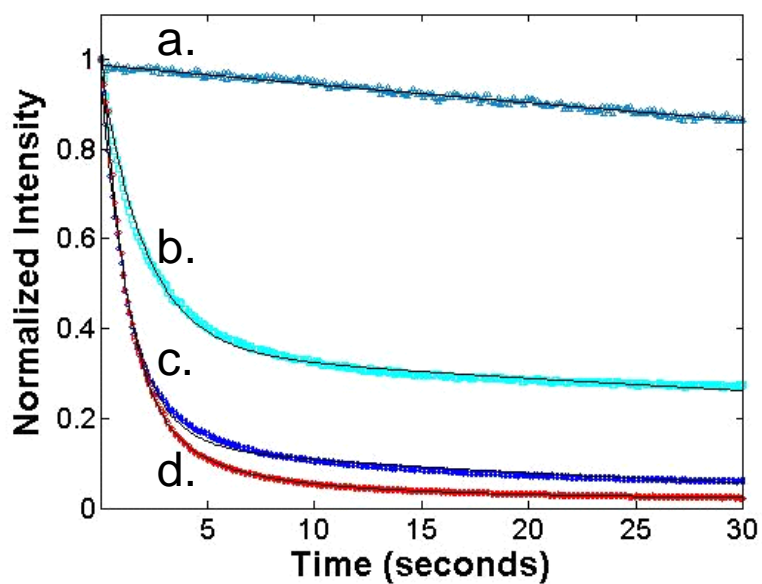


**Figure S3:** Normalized intensity decay curves for chemiluminescence signal after 5 second low power microwave exposure for (a) center of Al triangle; (b) glass substrate; (c) tip of aluminum triangle and (d) in the 1 mm gap of the ‘bow-tie’ geometry. Reaction decay rates were fit to a multi-exponential decay model,  $I(t) = \sum_i A_i e^{-k_i t}$ .

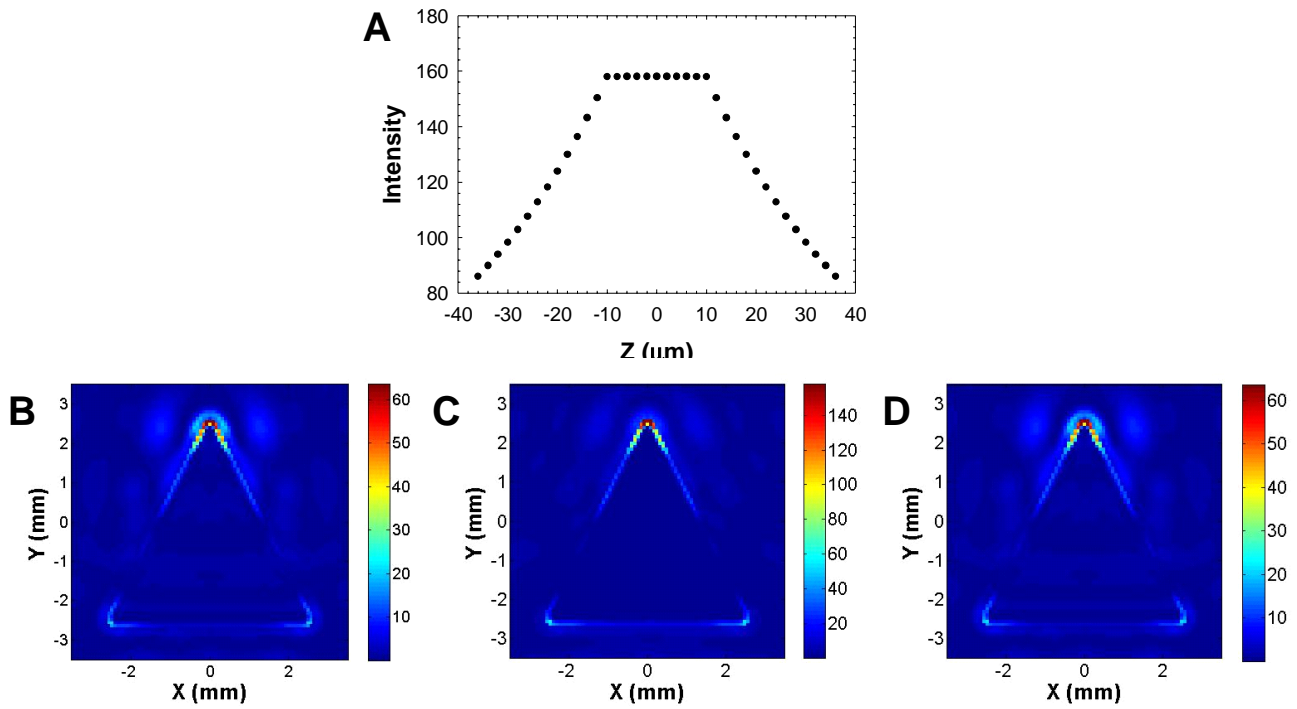


**Figure S4:** A) Simulated field intensity ( $I_x + I_y$ ) distribution in the z plane for a TE polarized 2.45 GHz total field scattered field source incident upon a 3D 5 mm equilateral triangle 0.10 mm thick, whereby the x,y,z mesh sizes are 10, 10, and 2.5  $\mu\text{m}$  respectively. The triangle regions are modeled as perfect conductors and simulated images represent field distributions for cross sections in the z-plane at **B)** -40, **C)** 0, and **D)** 40  $\mu\text{m}$ .

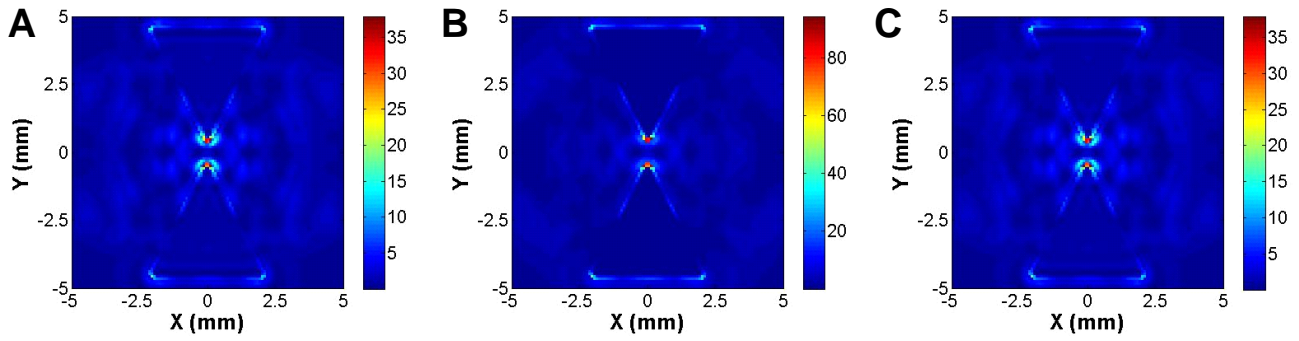


**Figure S5:** Simulated field intensity ( $I_x + I_y$ ) distribution in the  $z$  plane for a TE polarized 2.45 GHz total field scattered field source incident upon a 3D disjointed ‘bow-tie’ geometry composed of (2) 5 mm equilateral triangles 0.10 mm thick with a 1 mm gap size, whereby the  $x,y,z$  mesh sizes are 10, 10, and 2.5  $\mu\text{m}$  respectively. The triangle regions are modeled as perfect conductors and simulated images represent field distributions for cross sections in the  $z$ -plane at **A)** -0.40, **B)** 0, and **C)** 40  $\mu\text{m}$ .

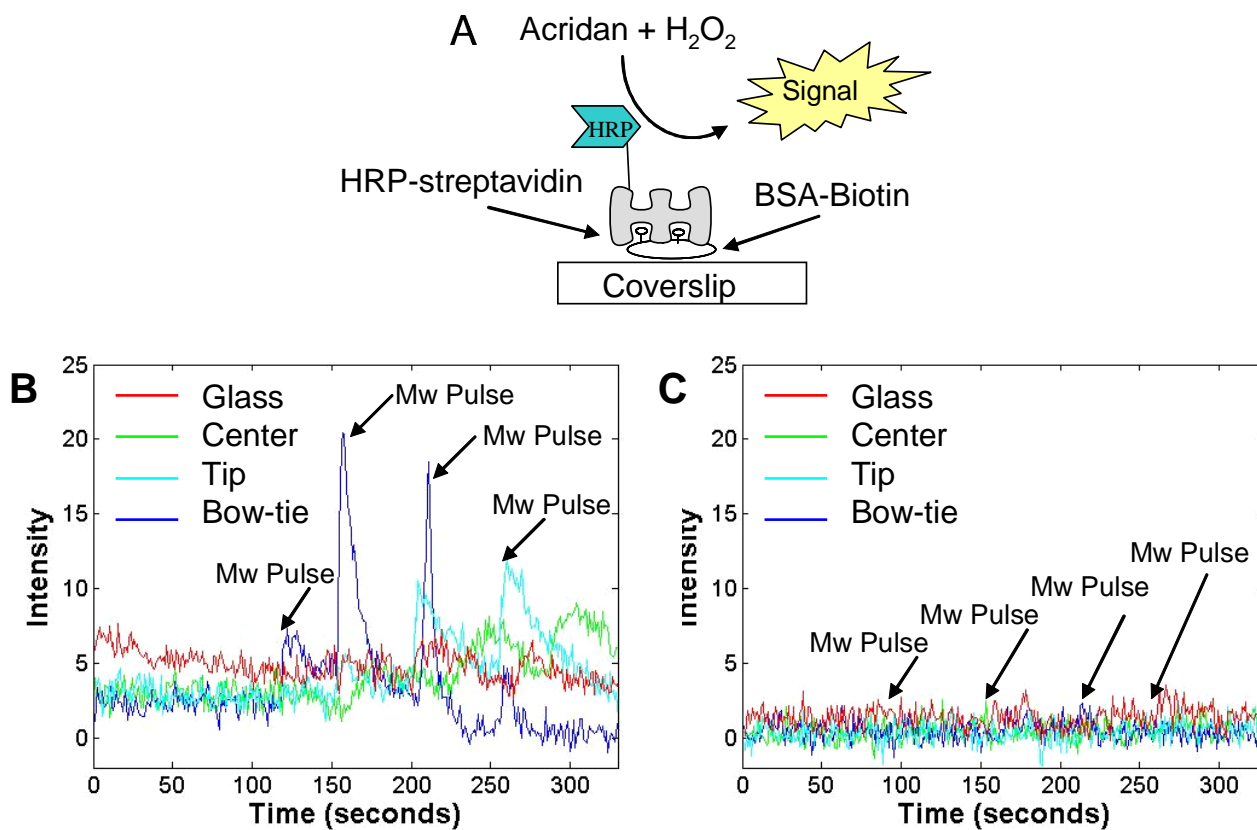


**Figure S6:** A) Model BSA-biotin, HRP-streptavidin chemiluminescent assay scheme. B) Acridan chemiluminescence emission as a function of time from HRP modified glass coverslips coated treated with 1  $\mu$ M BSA-biotin and 1  $\mu$ M HRP-streptavidin and positioned glass substrate geometries with and without 12.3 cm Al triangle 75 nm thick (left). C) Acridan chemiluminescence background emission as a function of time for glass coverslips incubated with 1.5% BSA and 1  $\mu$ M HRP-streptavidin (control) positioned on glass substrate geometries with and without 12.3 cm Al triangle 75 nm thick shapes (right). All samples were exposed to four 10 second microwave pulses (Mw pulse) at 10% power.

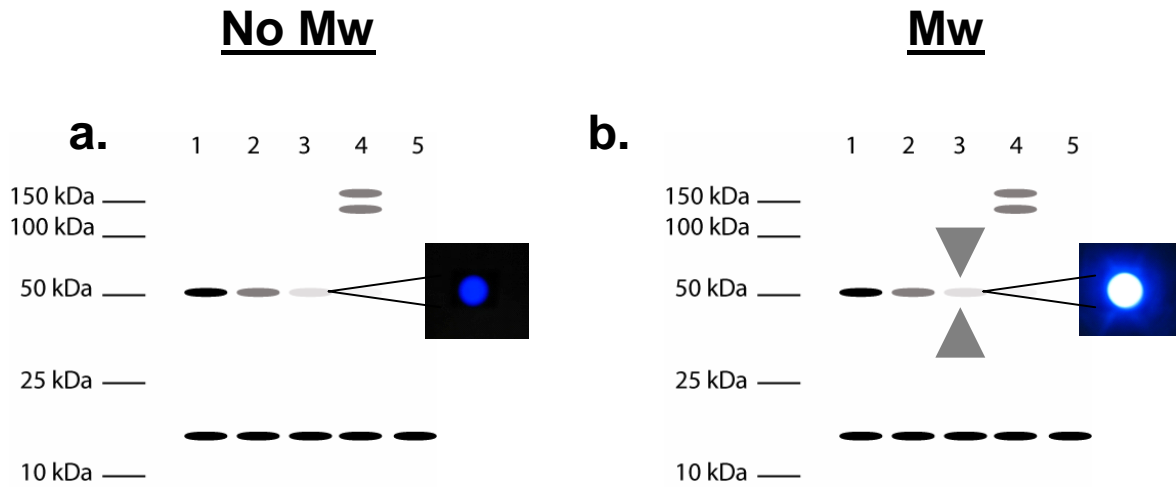


**Figure S7:** Cartoon illustrating a *potential* application of the technology: amplifying dim bands from a hypothetical Western blot scheme, whereby weak chemiluminescence signal from a Western blot (**A**) without affixed triangle geometries (left, inset) can be hypothetically amplified (**B**) with a disjointed ‘bow-tie’ geometry attached.